

2021

## Development and Characterization of Nb<sub>3</sub>N/Al<sub>2</sub>O<sub>3</sub> Superconducting Multilayers for Particle Accelerators

Chris Sundahl

Junki Makita  
*Old Dominion University*


Paul B. Welander

Yi-Feng Su

Fumitake Kametani

*See next page for additional authors*

Follow this and additional works at: [https://digitalcommons.odu.edu/physics\\_fac\\_pubs](https://digitalcommons.odu.edu/physics_fac_pubs)

 Part of the [Biological and Chemical Physics Commons](#), [Elementary Particles and Fields and String Theory Commons](#), [Engineering Physics Commons](#), and the [Mechanical Engineering Commons](#)

---

### Original Publication Citation

Sundahl, C., Makita, J., Welander, P. B., Su, Y.-F., Kametani, F., Xie, L., Zhang, H., Li, L., Gurevich, A., & Eom, C.-B. (2021). Development and characterization of Nb<sub>3</sub>N/Al<sub>2</sub>O<sub>3</sub> superconducting multilayers for particle accelerators. *Scientific Reports*, 11(1), 1-9, Article 7770. <https://doi.org/10.1038/s41598-021-87119-9>

This Article is brought to you for free and open access by the Physics at ODU Digital Commons. It has been accepted for inclusion in Physics Faculty Publications by an authorized administrator of ODU Digital Commons. For more information, please contact [digitalcommons@odu.edu](mailto:digitalcommons@odu.edu).

---

**Authors**

Chris Sundahl, Junki Makita, Paul B. Welander, Yi-Feng Su, Fumitake Kametani, Lin Xie, Huimin Zhang, Lian Li, Alex Gurevich, and Chang-Beom Eom



OPEN

## Development and characterization of Nb<sub>3</sub>Sn/Al<sub>2</sub>O<sub>3</sub> superconducting multilayers for particle accelerators

Chris Sundahl<sup>1</sup>, Junki Makita<sup>2</sup>, Paul B. Welander<sup>3</sup>, Yi-Feng Su<sup>4</sup>, Fumitake Kametani<sup>4,5</sup>, Lin Xie<sup>6</sup>, Huimin Zhang<sup>7</sup>, Lian Li<sup>7</sup>, Alex Gurevich<sup>2✉</sup> & Chang-Beom Eom<sup>1✉</sup>

Superconducting radio-frequency (SRF) resonator cavities provide extremely high quality factors  $> 10^{10}$  at 1–2 GHz and 2 K in large linear accelerators of high-energy particles. The maximum accelerating field of SRF cavities is limited by penetration of vortices into the superconductor. Present state-of-the-art Nb cavities can withstand up to 50 MV/m accelerating gradients and magnetic fields of 200–240 mT which destroy the low-dissipative Meissner state. Achieving higher accelerating gradients requires superconductors with higher thermodynamic critical fields, of which Nb<sub>3</sub>Sn has emerged as a leading material for the next generation accelerators. To overcome the problem of low vortex penetration field in Nb<sub>3</sub>Sn, it has been proposed to coat Nb cavities with thin film Nb<sub>3</sub>Sn multilayers with dielectric interlayers. Here, we report the growth and multi-technique characterization of stoichiometric Nb<sub>3</sub>Sn/Al<sub>2</sub>O<sub>3</sub> multilayers with good superconducting and RF properties. We developed an adsorption-controlled growth process by co-sputtering Nb and Sn at high temperatures with a high overpressure of Sn. The cross-sectional scanning electron transmission microscope images show no interdiffusion between Al<sub>2</sub>O<sub>3</sub> and Nb<sub>3</sub>Sn. Low-field RF measurements suggest that our multilayers have quality factor comparable with cavity-grade Nb at 4.2 K. These results provide a materials platform for the development and optimization of high-performance SIS multilayers which could overcome the intrinsic limits of the Nb cavity technology.

For decades, Nb has been the material of choice for the radio-frequency superconducting (SRF) resonators for high-energy particle accelerators. Technological advances have resulted in the development of Nb cavities which can exhibit extremely high quality factors  $Q > 10^{10}$  @ 1–2 GHz and 2 K while sustaining accelerating gradients up to 50 MV/m<sup>1–3</sup>. Such exemplary performance and low RF losses can only be achieved if the cavities operate in a Meissner state which can persist up to the maximum magnetic field at the inner cavity surface reaches the superheating field  $B_s = 240 \text{ mT}^{1–3}$ . At  $B = B_s$  the low-dissipative Meissner state becomes absolutely unstable with respect to dissipative penetration of vortices, causing an explosive increase of RF power and thermal quench of the cavity. The state-of-the-art Nb cavities can already operate at the peak magnetic field close to  $B_s$ , thus, increasing accelerating gradients beyond the intrinsic limits of Nb requires materials with higher  $B_s$ . There are many such materials but all of them are type-II superconductors with lower critical field  $B_{c1}$  smaller than  $B_{c1} \approx 170–180 \text{ mT}$  of Nb which makes high- $B_s$  superconductors prone to detrimental penetration of vortices at low fields<sup>4,5</sup>. To overcome this problem, it was proposed to nanostructure the inner surface of Nb cavities by coating it with multilayers of thin superconductors (S) separated by dielectric insulating (I) layers (Fig. 1)<sup>6</sup>. Here the S-layer material has a superheating field  $B_s$  higher than  $B_{s0}$  of Nb, whereas the thickness  $d$  of S layers is smaller than the London penetration depth  $\lambda$ , and the thickness of I layers can be a few nm to suppress the interlayer Josephson coupling. Such SIS structures greatly increase barriers for penetration of vortices in the bulk of the cavity which could potentially withstand the RF fields limited by the superheating field of S-layer. For instance, using Nb<sub>3</sub>Sn with  $B_s = 480 \text{ mT}$  could nearly double the maximum accelerating gradient as compared to the best Nb cavities. The multilayer approach is based on the lack of thermodynamically stable parallel vortices in thin decoupled S

<sup>1</sup>Department of Materials Science and Engineering, University of Wisconsin-Madison, Madison, WI 53706, USA. <sup>2</sup>Physics Department and Center for Accelerator Science, Old Dominion University, Norfolk, VA 23529, USA. <sup>3</sup>SLAC National Accelerator Laboratory, Menlo Park, CA 94025, USA. <sup>4</sup>Applied Superconductivity Center, National High Magnetic Field Laboratory, Florida State University, Tallahassee, FL 32310, USA. <sup>5</sup>Department of Mechanical Engineering, FAMU-FSU College of Engineering, Tallahassee, FL 32310, USA. <sup>6</sup>Department of Physics, Southern University of Science and Technology, Shenzhen 518055, China. <sup>7</sup>Department of Physics and Astronomy, West Virginia University, Morgantown, WV 26506, USA. ✉email: agurevic@odu.edu; eom@engr.wisc.edu

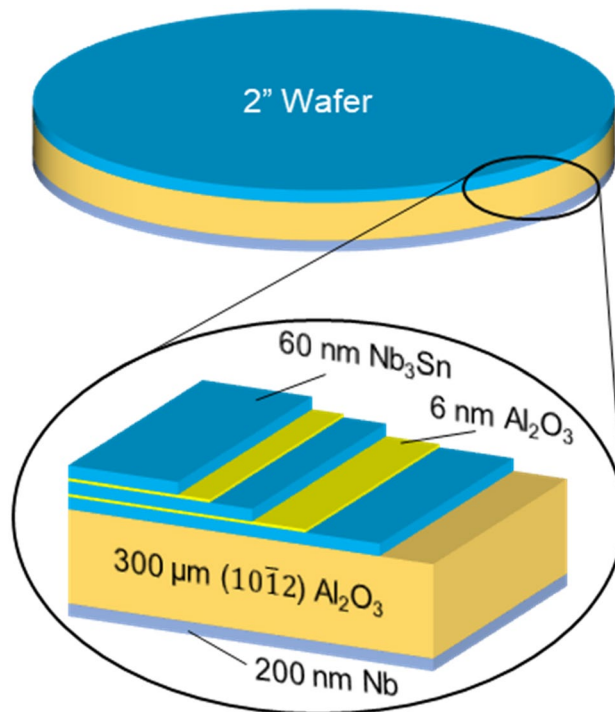


**Figure 1.** Schematic of Nb<sub>3</sub>Sn/Al<sub>2</sub>O<sub>3</sub> multilayer heterostructures on Al<sub>2</sub>O<sub>3</sub> wafer. Back side of Al<sub>2</sub>O<sub>3</sub> wafer is coated with a thick Nb film.

screens at  $B < B_{c1}$  where  $B_{c1}$  is strongly enhanced in films with  $d < \lambda^{6-10}$ . Because the inner surface of the Nb cavity is partially screened by multilayers, both  $Q(H)$  and the breakdown field can be increased due to lower surface resistance  $R_s$  and higher  $H_c$  of the layer material<sup>6</sup>.

The multilayer coating, which opens up a principal opportunity to break the Nb monopoly in SRF cavities, has been tested by several groups using MgB<sub>2</sub>, Nb<sub>3</sub>Sn, NbN, NbTiN, and dirty Nb as coating materials. These experiments have shown an increase of the dc field onset of penetration of vortices on Nb surfaces coated with different SIS structures<sup>4,11-19</sup>, although such key SRF characteristics as the surface resistance and quality factors of SIS multilayers under high-amplitude RF fields have been investigated to a much lesser extent. The first results on low-field Q measurements on NbN/MgO multilayers<sup>13,19</sup> have shown that SIS multilayers can have lower  $R_s$  than bulk Nb. However, the SRF performance of Nb<sub>3</sub>Sn, the current material of choice for the next generation coating material<sup>20</sup>, has not yet been investigated in SIS structures. The development of SIS structures requires overcoming many materials science and technological challenges to achieve good superconducting properties and SRF performance while providing optimal stoichiometry and morphology of the layers and the interfaces and transparency of grain boundaries to extremely high RF current densities. In this work we report results on growth and characterizations of Nb<sub>3</sub>Sn/Al<sub>2</sub>O<sub>3</sub> multilayers which exhibit good superconducting properties and low-field SRF performance on par with the cavity-grade Nb.

## Results and discussion

**Multilayer growth.** We developed a technique of high-temperature confocal sputtering of Nb and Sn from elemental targets to grow stoichiometric Nb<sub>3</sub>Sn multilayers with Al<sub>2</sub>O<sub>3</sub> interlayers. Details are given in the Supplemental Information. Thin films and multilayers of different thicknesses were grown on different sapphire single crystal substrates for the subsequent characterizations. For instance, 60 nm thick Nb<sub>3</sub>Sn films were grown on 10 × 10 mm sapphire substrates for transport, scanning tunneling spectroscopy and electron microscopy characterizations. For RF tests, we grew Nb<sub>3</sub>Sn/Al<sub>2</sub>O<sub>3</sub> multilayers on 2" diameter sapphire wafers (R-plane, 300 μm thick). These multilayers had up to three 60 nm Nb<sub>3</sub>Sn layers separated by 6 nm Al<sub>2</sub>O<sub>3</sub>. The thickness of the Nb<sub>3</sub>Sn layers was chosen to be smaller than the London penetration depth<sup>5,6</sup>. A 200 nm thick Nb film was deposited on the backside of the wafers to prevent leakage of RF field during cavity measurements. The geometry of multilayer samples used in our RF measurements of quality factors is shown in Fig. 1.

The Nb-Sn phase diagram contains several line compounds. For instance, Nb<sub>3</sub>Sn and Nb<sub>6</sub>Sn<sub>5</sub> coexist in the region marked in Fig. 2a. Here a low- $T_c$  Nb<sub>6</sub>Sn<sub>5</sub> phase is clearly undesirable in these films<sup>21</sup>. Within the Nb<sub>3</sub>Sn phase region extending from 17 to 25% Sn, the critical temperature  $T_c$  degrades steeply as stoichiometry moves away from a 3:1 ratio<sup>22</sup>. These two conditions demand that Nb<sub>3</sub>Sn films should contain 25% of Sn. This was accomplished by providing processing conditions reflecting the field in the upper right of the phase diagram in Fig. 2a, a two-phase region containing only stoichiometric Nb<sub>3</sub>Sn and liquid Sn. Films were grown by confocal sputtering of Nb and Sn from elemental targets. By providing a large over-pressure of Sn at high growth temperatures, it has been found that the ratio of Nb:Sn can be pinned at 3:1. The abundance of Sn drives the

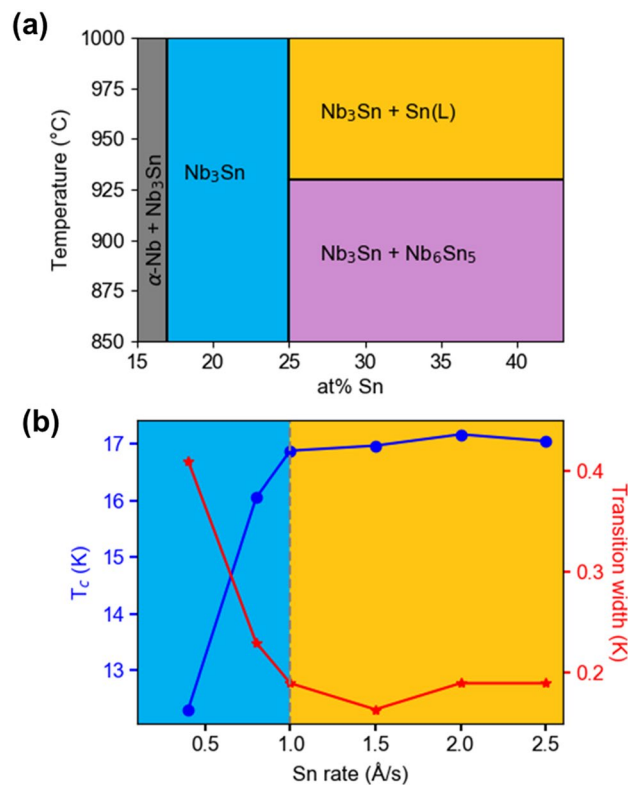


**Figure 2.** Connecting the Nb-Sn phase diagram to electrical properties and process window. (a) Relevant adsorption-controlled growth regime (orange) of Nb-Sn phase diagram. Nb<sub>3</sub>Sn spans 17–25% Sn, and the desired Nb<sub>3</sub>Sn + liquid Sn field lies above 930 °C and 25% Sn. (b)  $T_c$ ,  $\Delta T_c$  vs the Sn flux of 60 nm thick Nb<sub>3</sub>Sn single layer thin films on Al<sub>2</sub>O<sub>3</sub> substrates.  $T_c$  levels off above 1.0 Å/s Sn, corresponding to the adsorption-controlled growth window and the film composition reach 25% Sn.

material into the two-phase region, where excess Sn re-evaporates from the film, avoiding the formation of Sn precipitates<sup>23,24</sup>. To achieve the high temperatures (>930 °C) required for this growth, sapphire substrates were heated from behind with a SiC radiative heater. Radiation passed through the substrate and heated the depositing metal directly. Growth temperature was measured by pyrometer. Details of the film growth are given in the Supplemental Information.

A series of films was grown with fixed Nb flux (0.7 Å/s) and varying Sn flux (0.4–2.5 Å/s), and low-temperature resistance measurements were carried out to find the window for this self-regulating adsorption-controlled process. Shown in Fig. 2b are the dependencies of the critical temperature  $T_c$  and transition width  $\Delta T_c$  on the deposition rate of Sn which clearly saturate at ~1 Å/s. Given the dependence of  $T_c$  on Sn content in Nb<sub>3</sub>Sn, this growth rate roughly corresponds to the boundary between two processing regimes. At lower flux, Sn evaporates from the film faster than it can be incorporated, resulting in a Sn-deficient film. At higher flux, sufficient Sn is provided to react with all available Nb, and only excess Sn re-evaporates.

The dielectric Al<sub>2</sub>O<sub>3</sub> interlayers were grown after allowing Nb<sub>3</sub>Sn to cool down to <400 °C, using a single stoichiometric target with RF power at a rate of 1.8 nm/min without any further heating applied to the substrate. Depositing under these conditions protects the SiC heater element from oxygen evolved during the sputtering process and prevents undesired reactions with the Nb<sub>3</sub>Sn surface. This Nb<sub>3</sub>Sn/Al<sub>2</sub>O<sub>3</sub> stack was then heated again to above 900 °C, which allows the Al<sub>2</sub>O<sub>3</sub> to crystallize, and the process was repeated to grow heterostructures of up to three Nb<sub>3</sub>Sn layers. The chamber setup and growth steps are depicted in Fig. 3.

**Structural characterization.** A SIS sample with three Nb<sub>3</sub>Sn layers was prepared for analysis by cross-sectional scanning transmission electron microscopy (STEM). A low-magnification image (Fig. 4a) represents the morphology and nanostructure of the stack. Each Nb<sub>3</sub>Sn layer is polycrystalline with irregular interfaces and grain size is 20–100 nm along the film surface direction. The Al<sub>2</sub>O<sub>3</sub> layers conform closely to the layer below but are discontinuous along the Nb<sub>3</sub>Sn/Al<sub>2</sub>O<sub>3</sub> interface. Despite the repeated thermal cycling during stacking, it appears that the lower layers have not degraded in comparison to the top layer.

The chemical stability of these films is further confirmed by compositional mapping with energy dispersive spectroscopy (EDS) (Fig. 4b). Intensity of the Al K $\alpha$  and O K $\alpha$  peaks are mapped from the region shown on the left. Although the Al<sub>2</sub>O<sub>3</sub> layers are not continuous, Al and O are confined to the Al<sub>2</sub>O<sub>3</sub> layers, and do not mix with the Nb<sub>3</sub>Sn layers. The exception to this is the presence of O at the interface of the topmost Nb<sub>3</sub>Sn film with the atmosphere, where ambient conditions are sufficient to cause a reaction. A capping Al<sub>2</sub>O<sub>3</sub> layer could be deposited

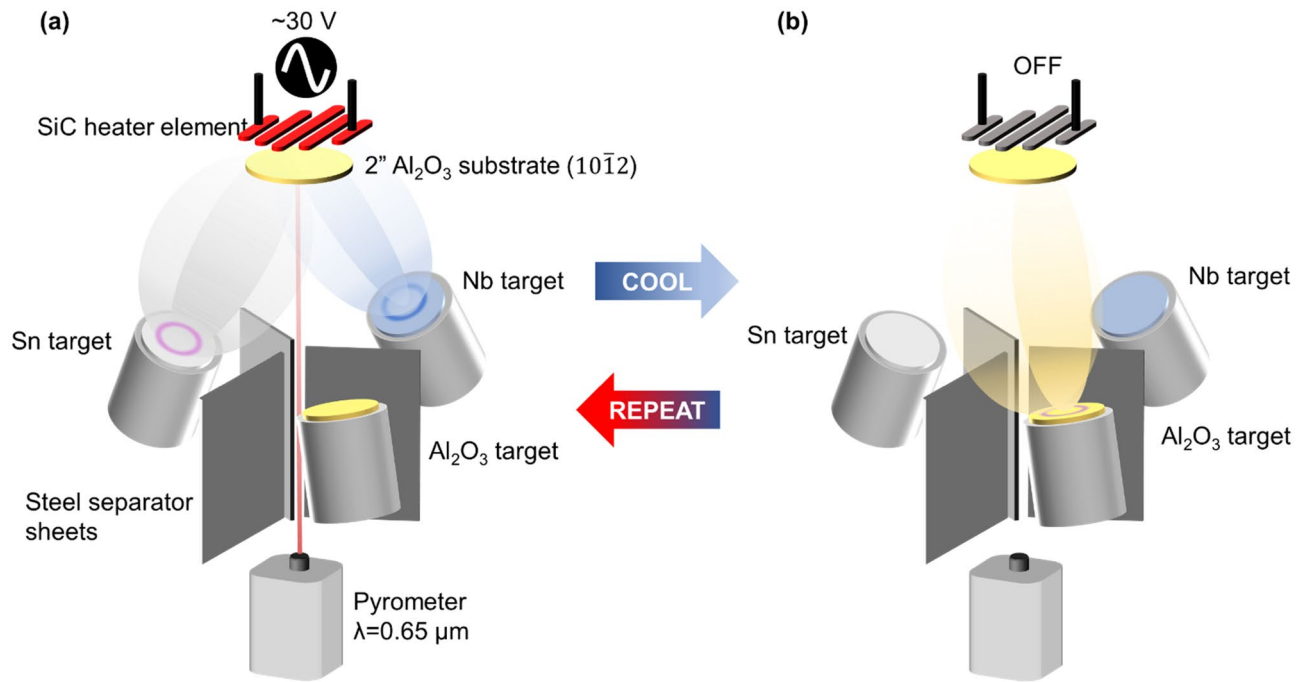


**Figure 3.** Schematic of thin films deposition setup and sequential processing steps for Nb<sub>3</sub>Sn/Al<sub>2</sub>O<sub>3</sub> multilayer heterostructures. (a) Nb and Sn are sputtered onto Al<sub>2</sub>O<sub>3</sub> substrate while heater element is powered on. (b) After allowing film to cool, Al<sub>2</sub>O<sub>3</sub> is sputtered from a single stoichiometric Al<sub>2</sub>O<sub>3</sub> target. Sample is heated again to anneal Al<sub>2</sub>O<sub>3</sub>. These two steps are repeated to produce multilayer samples.

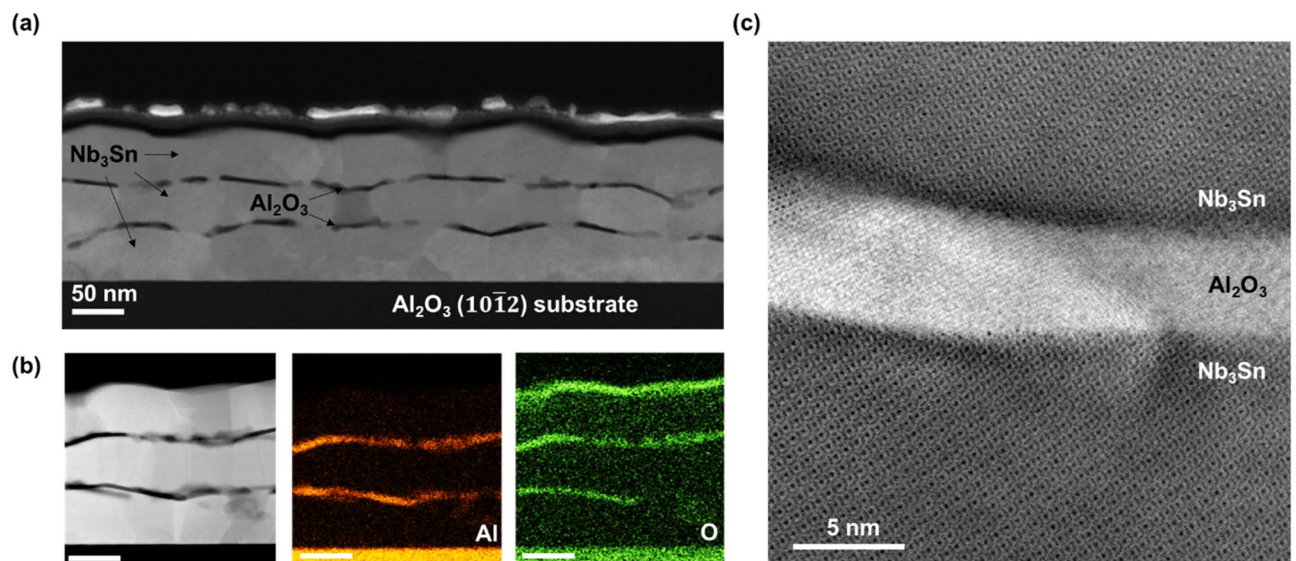


**Figure 4.** Cross-sectional transmission electron microscopy images of Nb<sub>3</sub>Sn/Al<sub>2</sub>O<sub>3</sub> multilayer heterostructures (a) Low-magnification image of trilayer morphology. (b) EDS compositional mapping of Al and O showing no interdiffusion between Al<sub>2</sub>O<sub>3</sub> and Nb<sub>3</sub>Sn. (c) High-magnification image of the interfaces between Al<sub>2</sub>O<sub>3</sub> and Nb<sub>3</sub>Sn.

to prevent this oxidation, but we did not use it for the multilayer samples described in this work. Note that the slight O signal in the Nb<sub>3</sub>Sn layers in Fig. 4b are due to the slight oxidation of the TEM specimen surface. As our RF cavity measurements show, these Al<sub>2</sub>O<sub>3</sub> layers do not contribute significantly to surface resistance at low fields.

A higher-magnification image of the S–I interface is shown in Fig. 4c. The atomic structure of Nb<sub>3</sub>Sn is well-preserved at the interface, suggesting that there is almost no diffusion or intermixing from the Al<sub>2</sub>O<sub>3</sub>. The lower Nb<sub>3</sub>Sn grain orients the [023] direction normal to the film surface, and this direction is also preserved in the upper Nb<sub>3</sub>Sn grain. This can occur when the upper Nb<sub>3</sub>Sn layer deposits with the same epitaxial relationship to the underlying Al<sub>2</sub>O<sub>3</sub> as the lower layer has with the Al<sub>2</sub>O<sub>3</sub> substrate. This structure can also form when a Nb<sub>3</sub>Sn

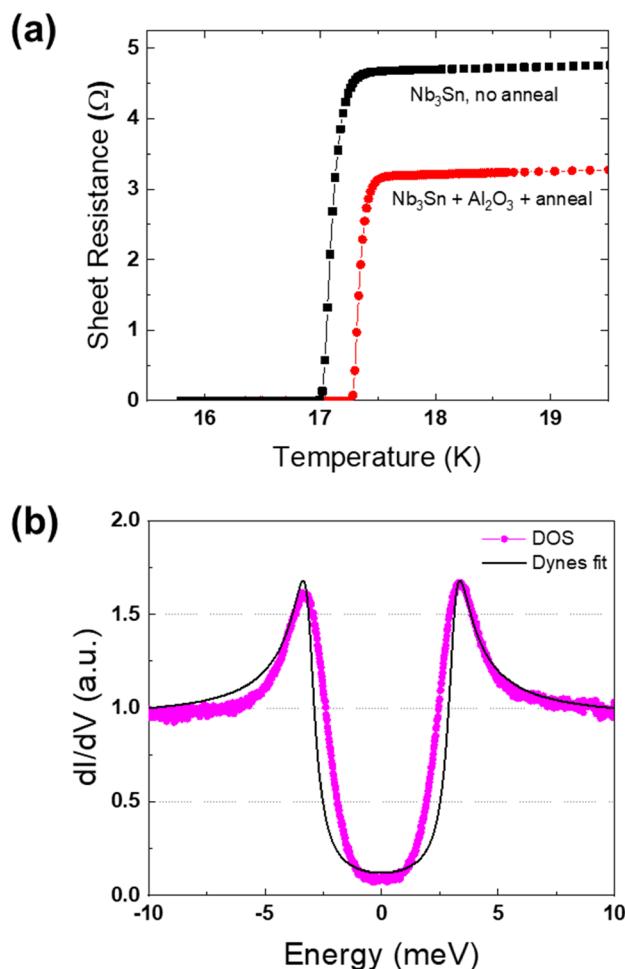


**Figure 5.** Superconducting properties of single-layer Nb<sub>3</sub>Sn films. **(a)** Resistive superconducting transition for two identical 60 nm thick films, one of which is capped with 6 nm Al<sub>2</sub>O<sub>3</sub> overlayer and annealed at 900 °C for 10 min. **(b)** Density of states measured by scanning tunneling spectroscopy and Dynes fit for a 60 nm thick Nb<sub>3</sub>Sn film.

grain nucleates on top of a Nb<sub>3</sub>Sn surface exposed by breaks in the discontinuous Al<sub>2</sub>O<sub>3</sub> layer. X-ray diffractometry indicates that Nb<sub>3</sub>Sn grains in the second layer have more random crystallographic orientation compared to the first layer (see the Supplemental material).

**Superconducting properties.** Our dc transport measurements have shown that the Nb<sub>3</sub>Sn films capped with Al<sub>2</sub>O<sub>3</sub> and annealed with no further deposition exhibit good superconducting properties. For instance, the superconducting resistive transitions of a bare Nb<sub>3</sub>Sn film and a Nb<sub>3</sub>Sn/Al<sub>2</sub>O<sub>3</sub> structure annealed at 900 °C for 10 min are shown in Fig. 5a. Here the critical temperature of the annealed sample is about 0.25 K higher than  $T_c$  of the unannealed sample, and residual resistivity ratio (RRR), an indicator of crystalline and metallic quality, is improved from 3.5 to 4.26. On the other hand, Nb<sub>3</sub>Sn films annealed *without* the Al<sub>2</sub>O<sub>3</sub> cap, even under high Sn flux to prevent evaporative loss, have degraded superconducting properties compared to an un-annealed film.

The superconducting properties essential for the RF performance were characterized by scanning tunneling spectroscopy (STS) which measures the differential tunneling conductance  $dI/dV$  proportional to the quasi-particle density of states (DOS),  $N(E)$ . Shown in Fig. 5b is a representative tunneling spectrum measured in the center of a Nb<sub>3</sub>Sn grain at 4 K. The DOS curves, which clearly show the superconducting gap  $\Delta$  at the Fermi surface, were fit using the conventional Dynes model<sup>25,26</sup>:

$$N(E) = N_0 \operatorname{Re} \left[ \frac{E - i\Gamma}{\sqrt{(E - i\Gamma)^2 - \Delta^2}} \right] \quad (1)$$

where the phenomenological parameter  $\Gamma$  accounts for the broadening of the DOS peaks due to a finite lifetime of quasiparticles, and  $N_0$  is the DOS in the normal state. The fit was done with  $\Gamma = 0.4$  meV and  $\Delta \approx 3.1$  meV, consistent with the conventional gap value for a stoichiometric Nb<sub>3</sub>Sn<sup>4</sup>. The ratio  $\Gamma/\Delta \approx 13\%$  in our samples turns out to be about 2–3 times larger than the values observed by tunneling spectroscopy on 1–2  $\mu\text{m}$  thick

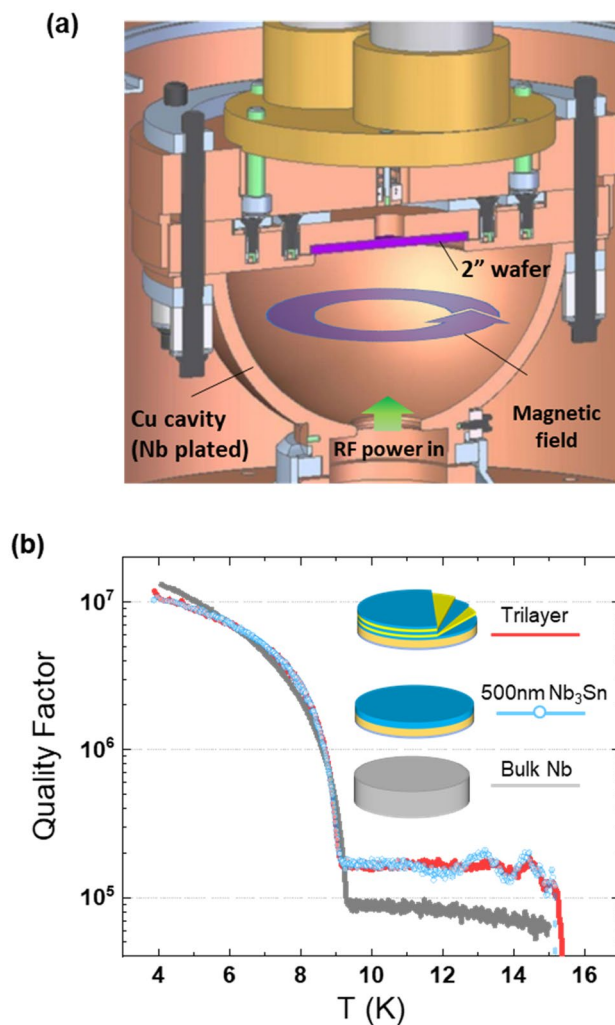


**Figure 6.** (a) Cutaway of hemispherical resonator cavity at SLAC used for these measurements. RF power is pumped in at the bottom, and magnetic field lines oscillate parallel to sample surface. (b) RF Surface resistance measurements of Nb<sub>3</sub>Sn film and multilayer compared to cavity-grade Nb.

Nb<sub>3</sub>Sn films for rf applications<sup>27</sup> and Nb coupons<sup>28</sup>. The deviations of the STM data from the Dynes model at low energies  $E < \Delta$  may indicate the effects of local non-stoichiometry, gap anisotropy and strain<sup>22</sup>, scattering of quasiparticles on magnetic impurities, and a thin layer with deteriorated superconducting properties at the surface<sup>27–30</sup>. In turn, the subgap quasiparticles states which appear at  $|E| < \Delta$  due to a finite  $\Gamma$  contribute to a temperature-independent residual surface resistance  $R_i$  at  $k_B T < \Delta$ <sup>5,29</sup>

$$R_i = \frac{\mu_0^2 \omega^2 \lambda^3 \Gamma^2}{2\rho_n (\Delta^2 + \Gamma^2)} \quad (2)$$

Here  $\mu_0$  is the permeability of free space,  $\rho_n$  is the normal-state resistivity,  $\lambda$  is the magnetic penetration depth, and  $\omega = 2\pi f$  is the circular RF frequency<sup>5</sup>. For  $\lambda = 120$  nm,  $\rho_n = 3.0 \times 10^{-7}$   $\Omega\text{m}$ , and the fit parameters  $\Delta = 3.1$  meV and  $\Gamma = 0.4$  meV, we obtain  $R_i \approx 5.0$  n $\Omega$  at  $f = 1.3$  GHz. This estimate is of the order of  $R_i \approx 5\text{--}10$  n $\Omega$  for large-grain Nb cavities<sup>31</sup>. Below a few nm thick surface layer but well within the rf penetration depth  $\lambda \approx 120$  nm, the gap peaks in the DOS are likely much sharper. There are other essential contributions to  $R_i$  most notably due to non-stoichiometric regions in the bulk<sup>27</sup>, grain boundaries and trapped vortices<sup>32</sup>.

**Low-field RF characterization.** Multilayer samples grown on 2" sapphire wafers were tested in a hemispherical Nb-coated cavity at SLAC National Accelerator Laboratory. The experimental setup was described previously<sup>33</sup>. A rendering of this cavity is shown in Fig. 6a. The cavity operates in a TE<sub>032</sub>-like mode at 11.4 GHz and the surface RF field of the order of 30  $\mu\text{T}$ , with a pocket on the flat face for mounting 2"-diameter samples (shown in purple). The overall cavity quality factor is measured, and the properties of the wafer can be deduced by comparison with known samples. The geometry of the cavity is engineered such that the magnetic field is strongest at the sample surface, limiting the contribution of the cavity material to the overall cavity loss. Accord-



ing to simulations, the participation factor is 0.33 for the 2"-diameter sample. Crucially, the magnetic field at the sample is in the radial direction and parallel to the sample surface, making it possible to measure RF properties of the sample without interference from the perpendicular component of the field. Low-field measurements of  $Q(T)$  of a Nb<sub>3</sub>Sn film in an uncoated Cu cavity are presented in the Supplementary Information.

The SRF performance of two Nb<sub>3</sub>Sn samples were compared in this system to a cavity-grade bulk Nb coupon. A 500 nm (~4λ) Nb<sub>3</sub>Sn film intended to completely screen out the RF magnetic field, and a 3 × 60 nm Nb<sub>3</sub>Sn/Al<sub>2</sub>O<sub>3</sub> trilayer were tested under the RF field. Both samples were coated with a 200 nm Nb film on the backside of the wafer to prevent leakage of magnetic field as shown in Fig. 1. The quality factor of the cavity with each sample, measured at low power with a network analyzer, is plotted in Fig. 6b. The abrupt increase in  $Q$  at about 15 K corresponds to the superconducting transition of Nb<sub>3</sub>Sn, followed by an increase of  $Q(T)$  at  $T_c = 9$  K of the Nb-coated host cavity.

As shown in Fig. 6b, the thick Nb<sub>3</sub>Sn film and the trilayer have nearly identical  $Q$  at  $T < 9$  K, indicating that Al<sub>2</sub>O<sub>3</sub> dielectric layers and interfaces do not contribute significantly to the RF dissipation. We would expect the thick Nb<sub>3</sub>Sn film to have a higher  $Q$ , as magnetic field is more fully screened before reaching the substrate and backside, so this result suggests that the maximum  $Q$  of these films and multilayers is limited by the quality of the Nb<sub>3</sub>Sn material rather than by the interfaces with Al<sub>2</sub>O<sub>3</sub>. The quality factors of both the film and the trilayer samples exceed  $Q(T)$  of Nb at  $T > 6$  K due to the higher  $T_c$  of Nb<sub>3</sub>Sn and is about 2 times smaller than  $Q$  of Nb at 4 K.

**Discussion.** The results of this work show that, despite the obvious non-stoichiometry and inhomogeneity of superconducting properties, grain boundaries, Nb inclusions, and incomplete Al<sub>2</sub>O<sub>3</sub> layers, our multilayers exhibit the quality factors on par of those of cavity-grade bulk Nb at 4 K and low RF power. The significant local non-stoichiometry of thick (a few micron) polycrystalline Nb<sub>3</sub>Sn coatings of Nb cavities<sup>20,27</sup>, as well as Sn depletion at grain boundaries in Nb<sub>3</sub>Sn<sup>34–37</sup> have been well documented in the literature. Yet, despite these materials issues which are also characteristic of 1–3 μm thick Nb<sub>3</sub>Sn films used in SRF cavities<sup>38</sup>, our Nb<sub>3</sub>Sn SIS structures exhibit higher low-field  $Q$  values than Nb at  $T > 6$  K<sup>20</sup>, consistent with the larger superconducting energy gap  $\Delta_{\text{Nb}_3\text{Sn}} \approx 2\Delta_{\text{Nb}}$  and a lower BCS surface resistance  $R_{\text{BCS}} \propto \omega^2 \rho_n^{1/2} e^{-\Delta/k_B T}$  of Nb<sub>3</sub>Sn. These experimental results not only show a remarkable resilience of low-field quality factors of Nb<sub>3</sub>Sn to the significant non-stoichiometry and materials imperfections but also suggest that the SRF performance of Nb<sub>3</sub>Sn coatings can be further improved by materials treatments. Our Nb<sub>3</sub>Sn multilayers exhibit a similar resilience of the low-power SRF performance to the materials imperfections.

The slopes of  $Q(T)$  for both the Nb<sub>3</sub>Sn film and multilayer shown in Fig. 5 tend to level off at 4–5 K and are clearly smaller than the slope of  $Q(T)$  for Nb. This indicates that  $Q(T)$  of the Nb<sub>3</sub>Sn samples at  $T = 4$ –5 K is not limited by the BCS surface resistance for which the slope of  $Q(T) \propto e^{\Delta/k_B T}$  for Nb<sub>3</sub>Sn would be larger than for Nb because  $\Delta_{\text{Nb}_3\text{Sn}} \approx 2\Delta_{\text{Nb}}$ . The behavior of  $Q(T)$  of the Nb<sub>3</sub>Sn samples at 4–5 K is thus indicative of a significant residual surface resistance caused by the multiphase structure of the films and multilayers and trapped vortices. Yet  $Q_0 \approx 10^7$  observed on our Nb<sub>3</sub>Sn multilayers at 11.4 GHz and 4 K suggests values of  $Q_0 \sim 10^9$  at 4 K and 1 GHz given the frequency dependence  $Q \propto \omega^{-2}$  which comes from the BCS surface resistance<sup>1–3</sup>, ohmic losses in metallic precipitates smaller than the RF skin depth and perhaps Josephson vortices trapped on grain boundaries<sup>39</sup>.

SRF performance at high RF fields and breakdown fields of Nb<sub>3</sub>Sn/Al<sub>2</sub>O<sub>3</sub> multilayers are yet to be explored. Generally, the effects of nonstoichiometry, proximity-coupled normal precipitates and weakly-coupled grain boundaries become more pronounced at higher RF fields. For instance, nonstoichiometric grain boundaries in Nb<sub>3</sub>Sn have been identified as prime pinning centers for vortices in Nb<sub>3</sub>Sn wires for high-field dc magnets<sup>39</sup>. However, weakly-coupled grain boundaries in Nb<sub>3</sub>Sn coating layers would block RF currents and cause dissipative penetration of Josephson vortices at fields well below the superheating field<sup>40</sup>, and sub-stoichiometric regions in Nb<sub>3</sub>Sn-coated Nb cavities are suspected to play an important role in RF cavity quench<sup>27</sup>. At the same time, meandering and breaks in Al<sub>2</sub>O<sub>3</sub> layers shown in Fig. 4 may not be detrimental for SRF performance as the layers can still provide their main role of intercepting and pinning small vortex loops originating at surface structural defects<sup>5,8</sup> since the pinholes sizes 10–50 nm in the Al<sub>2</sub>O<sub>3</sub> layers are smaller than magnetic size of the vortex  $\lambda \approx 100$ –200 nm of Nb<sub>3</sub>Sn. The misaligned breaks with lateral sizes smaller than the Nb<sub>3</sub>Sn layer thickness in neighboring dielectric Al<sub>2</sub>O<sub>3</sub> layers are not expected to strongly deteriorate the SRF performance of multilayers. Such imperfect dielectric layers still produce effective pinning barriers against penetration of parallel vortices and arresting vortex semi-loops originating on surface materials defects, which is instrumental in the multilayer approach<sup>5,6</sup>. At the same time, the roughness and breaks in Al<sub>2</sub>O<sub>3</sub> interlayers, as well as the variable thickness of Nb<sub>3</sub>Sn layers can pin short perpendicular vortices and do not let them propagate along the layers under RF current, which is also beneficial for the SRF performance of multilayers<sup>5</sup>. Though Al<sub>2</sub>O<sub>3</sub> layers do not fully separate Nb<sub>3</sub>Sn layers, we found that a 500 nm thick Nb<sub>3</sub>Sn film had a quality factor identical to a multilayer with three 60 nm Nb<sub>3</sub>Sn layers separated by 6 nm Al<sub>2</sub>O<sub>3</sub>, and both had  $Q$  approximately 2 times lower than a cavity-grade Nb reference. This indicates that losses in the thin Al<sub>2</sub>O<sub>3</sub> and the oxide-metallic interfaces do not contribute much to the surface resistance of our multilayer samples.

## Conclusions

In summary, we have developed a self-regulating, adsorption-controlled process for growth of Nb<sub>3</sub>Sn films and Nb<sub>3</sub>Sn/Al<sub>2</sub>O<sub>3</sub> multilayers. We have produced and characterized multiple multilayer samples with up to four superconducting layers. Despite the detrimental effects of nonstoichiometry, grain boundaries and breaks in the meandering Al<sub>2</sub>O<sub>3</sub> interlayers, the SRF performance of our multilayers turned out to be on par with that of Nb films. The growth technique reported in this work provides a platform for further optimizations of the SRF properties of SIS high-performance multilayers for superconducting resonator applications.

## Methods

Film deposition was carried out in a vacuum chamber pumped down to  $3.0 \times 10^{-8}$  Torr before being backfilled with Ar. Nb<sub>3</sub>Sn films were sputtered from elemental Nb (99.95%) and Sn (99.99%) targets in 3 mTorr of Ar to maximize deposition rate, at a distance of 15.5 cm from the substrate to improve flux uniformity. DC power to the sputter guns was current-controlled, and deposition rate was measured with an in situ quartz crystal monitor prior to growth. Pyrometer reading of the SiC heating element at the beginning of growth was ~1250 °C, and dropped to around 905 °C after 60 nm was deposited. Al<sub>2</sub>O<sub>3</sub> was sputtered from a stoichiometric 2" diameter ceramic target after the pyrometer reading fell below 400 °C. After deposition, the temperature was ramped back up to a pyrometer reading of 905 °C over the course of 10 min. These two steps were repeated to produce the multilayers.

Scanning transmission electron microscope (STEM) imaging and elemental analysis were performed in a probe-corrected atomic resolution analytical electron microscope (JEM-ARM200cF, JEOL) with an energy dispersive X-ray spectroscopy (EDS) detector (X-Max<sup>N</sup> 100TLE SDD, Oxford Instruments).

Superconducting transitions were measured in a closed-loop He cooler using 4-point van der Pauw geometry on 10 × 10 mm samples. The critical temperature  $T_c$  is defined as the temperature at which the sheet resistance falls below 1% of its normal state value at 18 K. The transition width  $\Delta T_c$  is defined as a difference between  $T_c$  and the point at which the lines drawn through the normal-state resistance and transition region intersect.

Low-temperature scanning tunneling microscopy/spectroscopy (STM/S) measurements were carried out in a STM system (USM1300, UNISOKU) at 4 K using polycrystalline PtIr tips. The dI/dV spectra were acquired using standard lock-in technique by applying a bias modulation of 0.2 mV (r.m.s.) at 732 Hz.

## Data availability

The data that supports the findings of the work are in the manuscripts main text and Supplementary Information. Additional data are available from the corresponding author upon reasonable request.

Received: 20 January 2021; Accepted: 15 March 2021

Published online: 08 April 2021

## References

1. Padamsee, H., Knobloch, J. & Hays, T. *RF Superconductivity for Accelerators* (Wiley, 2008).
2. Gurevich, A. Superconducting radio-frequency fundamentals for particle accelerators. *Rev. Accel. Sci. Technol.* **05**, 119–146 (2012).
3. Padamsee, H. S. Superconducting radio-frequency cavities. *Annu. Rev. Nucl. Part. Sci.* **64**, 175–196 (2014).
4. Valente-Feliciano, A.-M. Superconducting RF materials other than bulk niobium: A review. *Supercond. Sci. Technol.* **29**, 113002 (2016).
5. Gurevich, A. Theory of RF superconductivity for resonant cavities. *Supercond. Sci. Technol.* **30**, 034004 (2017).
6. Gurevich, A. Enhancement of rf breakdown field of superconductors by multilayer coating. *Appl. Phys. Lett.* **88**, 012511 (2006).
7. Kubo, T., Iwashita, Y. & Saeki, T. Radio-frequency electromagnetic field and vortex penetration in multilayered superconductors. *Appl. Phys. Lett.* **104**, 032603 (2014).
8. Gurevich, A. Maximum screening fields of superconducting multilayer structures. *AIP Adv.* **5**, 017112 (2015).
9. Liarte, D. B. *et al.* Theoretical estimates of maximum fields in superconducting resonant radio frequency cavities: Stability theory, disorder, and laminates. *Supercond. Sci. Technol.* **30**, 033002 (2017).
10. Kubo, T. Multilayer coating for higher accelerating fields in superconducting radio-frequency cavities: A review of theoretical aspects. *Supercond. Sci. Technol.* **30**, 023001 (2017).
11. Antoine, C. Z. *et al.* Characterization of superconducting nanometric multilayer samples for superconducting rf applications: First evidence of magnetic screening effect. *Phys. Rev. Spec. Top. Accel. Beams* **13**, 121001 (2010).
12. Tajima, T. *et al.* Studies on thin film MgB<sub>2</sub> for applications to RF structures for particle accelerators. *AIP Conf. Proc.* **1435**, 297–304 (2012).
13. Antoine, C. Z., Villegier, J.-C. & Martinet, G. Study of nanometric superconducting multilayers for RF field screening applications. *Appl. Phys. Lett.* **102**, 102603 (2013).
14. Beringer, D. B. *et al.* Thickness dependence and enhancement of  $H_{c1}$  in epitaxial MgB<sub>2</sub> thin films. *IEEE Trans. Appl. Supercond.* **23**, 7500604–7500604 (2013).
15. Roach, W. M., Beringer, D. B., Li, Z., Clavero, C. & Lukaszew, R. A. Magnetic shielding larger than the lower critical field of niobium in multilayers. *IEEE Trans. Appl. Supercond.* **23**, 8600203–8600203 (2013).
16. Tan, T. *et al.* Enhancement of lower critical field by reducing the thickness of epitaxial and polycrystalline MgB<sub>2</sub> thin films. *APL Mater.* **3**, 041101 (2015).
17. Tan, T., Wolak, M. A., Xi, X. X., Tajima, T. & Civale, L. Magnesium diboride coated bulk niobium: A new approach to higher acceleration gradient. *Sci. Rep.* **6**, 35879 (2016).
18. Junginger, T., Wasserman, W. & Laxdal, R. E. Superheating in coated niobium. *Supercond. Sci. Technol.* **30**, 125012 (2017).
19. Antoine, C. Z. *et al.* Optimization of tailored multilayer superconductors for RF application and protection against premature vortex penetration. *Supercond. Sci. Technol.* **32**, 085005 (2019).
20. Posen, S. & Hall, D. L. Nb<sub>3</sub>Sn superconducting radiofrequency cavities: Fabrication, results, properties, and prospects. *Supercond. Sci. Technol.* **30**, 033004 (2017).
21. Charlesworth, J. P., Macphail, I. & Madsen, P. E. Experimental work on the niobium-tin constitution diagram and related studies. *J. Mater. Sci.* **5**, 580–603 (1970).
22. Godeke, A. A review of the properties of Nb<sub>3</sub>Sn and their variation with A15 composition, morphology and strain state. *Supercond. Sci. Technol.* **19**, R68–R80 (2006).
23. Allen, L. H., Anklam, W., Beasley, M. R., Hammond, R. H. & Turneaure, J. P. RF surface resistance in Nb<sub>3</sub>Sn thin films. *IEEE Trans. Magn.* **21**, 525–527 (1985).
24. Allen, L. H., Beasley, M. R., Hammond, R. H. & Turneaure, J. P. RF Surface resistance of Nb<sub>3</sub>Sn, NbZr, and NbN thin films. *IEEE Trans. Magn.* **23**, 1405–1408 (1987).
25. Dynes, R. C., Narayanamurti, V. & Garno, J. P. Direct measurement of quasiparticle-lifetime broadening in a strong-coupled superconductor. *Phys. Rev. Lett.* **41**, 1509–1512 (1978).
26. Dynes, R. C., Garno, J. P., Hertel, G. B. & Orlando, T. P. Tunneling study of superconductivity near the metal-insulator transition. *Phys. Rev. Lett.* **53**, 2437–2440 (1984).

27. Becker, C. *et al.* Analysis of Nb<sub>3</sub>Sn surface layers for superconducting radio frequency cavity applications. *Appl. Phys. Lett.* **106**, 082602 (2015).
28. Lechner, E. M. *et al.* Electron tunneling and X-ray photoelectron spectroscopy studies of the superconducting properties of nitrogen-doped niobium resonator cavities. *Phys. Rev. Appl.* **13**, 044044 (2020).
29. Gurevich, A. & Kubo, T. Surface impedance and optimum surface resistance of a superconductor with an imperfect surface. *Phys. Rev. B* **96**, 184515 (2017).
30. Proslir, T. *et al.* Tunneling study of cavity grade Nb: Possible magnetic scattering at the surface. *Appl. Phys. Lett.* **92**, 212505 (2008).
31. Visentin, B., Barthe, M. F., Moineau, V. & Desgardin, P. Involvement of hydrogen-vacancy complexes in the baking effect of niobium cavities. *Phys. Rev. Spec. Top. Accel. Beams* **13**, 052002 (2010).
32. Dhakal, P., Ciovati, G. & Gurevich, A. Flux expulsion in niobium superconducting radio-frequency cavities of different purity and essential contributions to the flux sensitivity. *Phys. Rev. Accel. Beams* **23**, 023102 (2020).
33. Welander, P., Franzi, M. & Tantawi, S. Cryogenic RF characterization of superconducting materials at SLAC with hemispherical cavities. In *Proceedings of SRF2015* 735–738 (2015).
34. Suenaga, M. & Jansen, W. Chemical compositions at and near the grain boundaries in bronze-processed superconducting Nb<sub>3</sub>Sn. *Appl. Phys. Lett.* **43**, 791–793 (1983).
35. Sandim, M. J. R. *et al.* Grain boundary segregation in a bronze-route Nb<sub>3</sub>Sn superconducting wire studied by atom probe tomography. *Supercond. Sci. Technol.* **26**, 055008 (2013).
36. Lee, J. *et al.* Atomic-scale analyses of Nb<sub>3</sub>Sn on Nb prepared by vapor diffusion for superconducting radiofrequency cavity applications: A correlative study. *Supercond. Sci. Technol.* **32**, 024001 (2019).
37. Lee, J. *et al.* Grain-boundary structure and segregation in Nb<sub>3</sub>Sn coatings on Nb for high-performance superconducting radio-frequency cavity applications. *Acta Mater.* **188**, 155–165 (2020).
38. Spina, T., Tennis, B. M., Lee, J., Seidman, D. N. & Posen, S. Development and understanding of Nb<sub>3</sub>Sn films for radiofrequency applications through a sample-host 9-cell cavity. *Supercond. Sci. Technol.* **34**, 015008 (2021).
39. Scanlan, R. M., Fietz, W. A. & Koch, E. F. Flux pinning centers in superconducting Nb<sub>3</sub>Sn. *J. Appl. Phys.* **46**, 2244–2249 (1975).
40. Sheikhzada, A. & Gurevich, A. Dynamic transition of vortices into phase slips and generation of vortex-antivortex pairs in thin film Josephson junctions under dc and ac currents. *Phys. Rev. B* **95**, 214507 (2017).

## Acknowledgements

This work was supported by the US Department of Energy under grant # DE-SC0010081-020. Work at West Virginia University was supported by the U.S. Department of Energy under Award # DE-SC0017632. Work at SLAC National Accelerator Laboratory was supported by the U.S. Department of Energy under contract # DE-AC02-76SF00515. The nanostructural characterizations were supported by the National High Magnetic Field Laboratory and the National Science Foundation under grant # NSF/DMR-1644779), and by the State of Florida.

## Author contributions

C.S. developed multilayer growth process and fabricated samples. J.M. participated in RF characterization. Y.S., F.K., and L.X. performed cross-sectional TEM characterization. H.Z. and L.L. performed low-temperature STM characterization. P.B.W. performed low-temperature RF surface resistance characterization. C.B.E and A.G. initiated and directed the project. C.S and A.G. wrote the manuscript with contributions from all authors.

## Competing interests

The authors declare no competing interests.

## Additional information

**Supplementary Information** The online version contains supplementary material available at <https://doi.org/10.1038/s41598-021-87119-9>.

**Correspondence** and requests for materials should be addressed to A.G. or C.-B.E.

**Reprints and permissions information** is available at [www.nature.com/reprints](http://www.nature.com/reprints).

**Publisher's note** Springer Nature remains neutral with regard to jurisdictional claims in published maps and institutional affiliations.



**Open Access** This article is licensed under a Creative Commons Attribution 4.0 International License, which permits use, sharing, adaptation, distribution and reproduction in any medium or format, as long as you give appropriate credit to the original author(s) and the source, provide a link to the Creative Commons licence, and indicate if changes were made. The images or other third party material in this article are included in the article's Creative Commons licence, unless indicated otherwise in a credit line to the material. If material is not included in the article's Creative Commons licence and your intended use is not permitted by statutory regulation or exceeds the permitted use, you will need to obtain permission directly from the copyright holder. To view a copy of this licence, visit <http://creativecommons.org/licenses/by/4.0/>.

© The Author(s) 2021